ACS Partner Journal

CHEMICAL & BIOMEDICAL IMAGING

Open Access

pubs.acs.org/ChemBioImaging

Article

USSGAN: Unsupervised Spectral and Spatial Attention-Based Generative Adversarial Network for Cholangiocarcinoma Detection[†]

Published as part of Chemical & Biomedical Imaging special issue "AI for Chemical and Biomedical Imaging".

Sikhakolli Sravan Kumar, Anuj Deshpande,* Pooja A. Nair, Suresh Aala, Sunil Chinnadurai, Vineela Chandra Dodda, Inbarasan Muniraj, Md. Abdul Latif Sarker, and Hala Mostafa*

Cite This: *Chem. Biomed. Imaging* 2025, 3, 876−887

Read Online

ACCESS | Metrics & More | Article Recommendations

ABSTRACT: Cholangiocarcinoma, a form of liver bile duct cancer, is challenging to detect due to its critically low 5-year survival rate. Conventional imaging modalities, such as Computed Tomography (CT) and Magnetic Resonance Imaging (MRI), are widely used, but recent advancements in Hyperspectral Imaging (HSI) offer a promising, non-invasive alternative for cancer diagnosis. However, supervised learning methods often require large annotated datasets that can be difficult to obtain. To alleviate this limitation, we propose an unsupervised learning strategy using Generative Adversarial Networks (GANs) for cholangiocarcinoma detection. This approach, named Unsupervised Spectral and Spatial Attention-based GAN (USSGAN), employs an unsupervised Spectral-Spatial attention-based GAN to classify and segment cancerous regions without relying on labeled training data. The integration of an adaptive step size into Tasmanian Devil Optimization (TDO) enhances the convergence speed and effectively captures diverse cancerous features. Enhanced Tasmanian Devil Optimization (ETDO) further improves segmentation performance, making the framework robust and computationally efficient. The proposed method was tested on a publicly available multidimensional choledochal cholangiocarcinoma dataset, achieving superior performance compared with existing techniques in the literature. USSGAN demonstrated high accuracy across key metrics such as overall accuracy (OA), average accuracy (AA), and Cohen's Kappa. Ablation studies confirmed the critical contributions of the proposed enhancements to the overall performance. With an overall accuracy of 98.03%, the USSGAN closely aligns with the assessments of experienced pathologists while maintaining minimal computational requirements. Its lightweight nature ensures real-time deployment, providing results within a minute, making it a practical and effective solution for clinical applications.

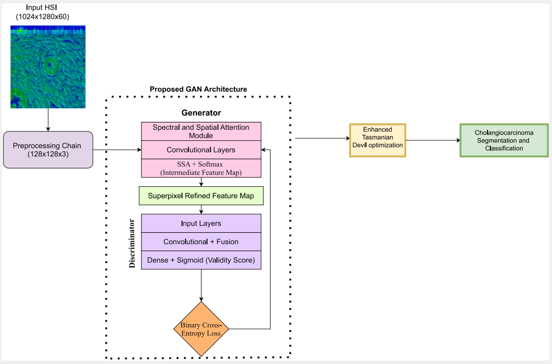

KEYWORDS: *hyperspectral imaging, cholangiocarcinoma, unsupervised learning, generative adversarial networks, enhanced tasmanian devil optimization*

■ INTRODUCTION

Cholangiocarcinoma, or liver bile duct cancer, is a rare yet formidable challenge in oncology due to its aggressive nature and critically low 5-year survival rate. Recent reports from the American Cancer Society have highlighted an alarming increase in its incidence, further emphasizing the need for early detection and effective diagnostic tools.[1] Based on its somatic location, cholangiocarcinoma is classified into two types: intrahepatic (occurring within the liver) and extrahepatic (occurring outside the liver). Extrahepatic cholangiocarcinoma, the most common and aggressive form, is further divided into perihilar (or Klatskin tumors) and distal types.[2,3] This study focused on Klatskin tumors, notorious for their complexity, which arise at the junction of the right and left bile ducts forming the common hepatic duct.

Traditional diagnostic techniques for cholangiocarcinoma include the CA 19−9 antigen blood test[4] and imaging modalities such as Computed Tomography (CT) and Magnetic Resonance Imaging (MRI).[5−7] Although these methods offer significant diagnostic capabilities, they are invasive, expensive, and often uncomfortable for patients. Hyperspectral Imaging (HSI) has emerged as a transformative technology, offering a noncontact, non-invasive diagnostic

Received: May 6, 2025
Revised: June 18, 2025
Accepted: June 27, 2025
Published: July 1, 2025

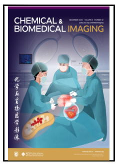

ACS Publications

https://doi.org/10.1021/cbmi.5c00054

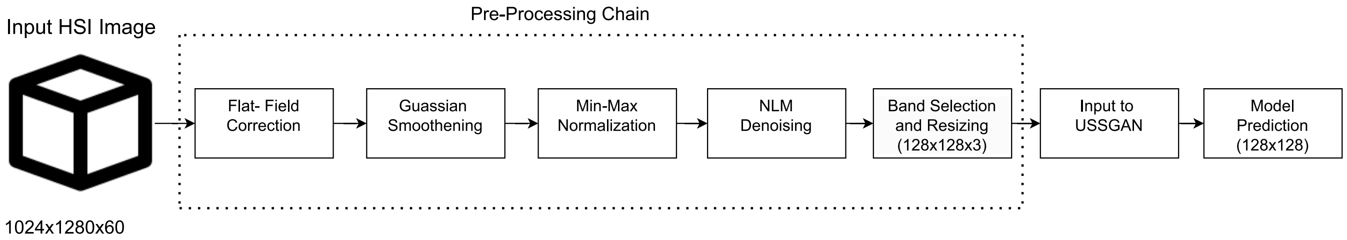

Figure 1. Preprocessing chain for hyperspectral image (HSI) processing: Flat-field correction to remove illumination artifacts, Gaussian smoothing for noise reduction, min-max normalization for intensity scaling, NLM denoising to preserve spatial details, band selection and redundancy elimination for feature optimization, followed by USSGAN for spectral-spatial segmentation and label prediction.

alternative. By capturing images in multiple hundreds of narrow spectral bands in the visible near-infrared (VNIR) region (400 to 1000 nm),[8,9] HSI enables the simultaneous acquisition of spatial and spectral information, making it particularly effective in identifying the chemical and physical attributes of biological tissues, including tumors. Beyond its application in medical imaging, HSI has been extensively utilized in remote sensing to address diverse challenges across various domains.[10−14] Historically, hyperspectral medical image classification has relied on pixel-level spectral features processed by classifiers, such as Support Vector Machines (SVM)[15] and logistic regression.[16] Although these traditional methods were pioneering, they struggled with redundancy and noise, resulting in suboptimal accuracy. The advent of deep learning marked a paradigm shift, with models like 3D U-Net achieving a remarkable classification accuracy of 94.38% for tumor segmentation.[17] Similarly, SAHIS-Net, which employs spectral attention modules and multiloss training, achieved a segmentation accuracy of 91.31%.[18] Recent deep learning models have continued to push the boundaries of medical HSI segmentation. MRANet[19] utilizes multipath residual attention blocks to enhance spatial feature learning while being robust to small training datasets. HCLA U-Net[20] incorporates high-level feature channel attention into a U-Net backbone, improving tumor delineation from hyperspectral microscopy images. MAEFNet[21] applies MLP-based attention modules within a U-Net framework to boost feature refinement and contextual encoding in biomedical segmentation tasks. However, these supervised learning (SL) approaches depend heavily on large labeled datasets, which are challenging to acquire and render computationally intensive.[22]

Semisupervised learning (SSL) bridges the gap between fully supervised and unsupervised methods by leveraging both labeled and unlabeled data.[23] Innovative SSL strategies have been explored in various contexts, such as Gui et al.,[24] who introduced a multistep dimensionality reduction method for tumor-related feature extraction from gene expression profiles. Xu et al.[25] proposed a heuristic SSL framework for subcellular location prediction using non-annotated cancer samples, while Thul et al.[26] developed a bioimage analysis system to detect mislocated proteins. Ma et al.[27] employed Affinity Network Fusion (ANF) for multiomic patient clustering, and Kumar et al.[28] achieved an F1-score of 71.18% using semisupervised hierarchical clustering on hyperspectral tissue images. Recently, our group proposed a statistical approach combining mean and median parameters, achieving digital annotations closely aligned with pathologists' labels, and yielding an SSIM of 94.14%.[29] Despite their promise, SSL methods still rely partly on labeled data, making their deployment in annotation-scarce scenarios difficult.

Unsupervised learning (USL) offers a pathway for overcoming these limitations by entirely eliminating the reliance on labeled data sets. Advanced USL methods, such as CNN-based approaches by Halicek et al.[30] and 3D CNNs developed by Wang et al.,[31] have shown improvements in tumor classification and segmentation. Wei et al.[32] employed deep autoencoders to extract spatial and spectral features, and Zeng et al.[33] proposed a fusion transformer for enhanced microscopic HSI classification. Muhammad et al.[34] introduced a convolutional autoencoder-based clustering framework, demonstrating the feasibility of unsupervised cholangiocarcinoma subtype discovery using hyperspectral microscopy. However, fully unsupervised approaches to cholangiocarcinoma detection are rare. For example, Wang et al.[35] introduced the Deep Margin Cosine Autoencoder (DMCA), which partially relies on labeled training data, limiting its applicability in real-world scenarios.

To address these gaps, we propose an unsupervised segmentation framework built on Generative Adversarial Networks (GANs). Generative Adversarial Networks (GANs)[36] are powerful frameworks that excel in various computer vision tasks, including image classification and segmentation.[37] For segmentation tasks, GANs effectively enhance the accuracy of predictions by refining feature maps and producing realistic and detailed segmentation outputs. Their ability to handle complex data distributions makes them particularly useful in challenging domains, such as hyperspectral imaging and medical image analysis.[38]

The proposed framework leverages spatial and spectral attention modules to capture intricate hyperspectral features, without using labeled data. Furthermore, the proposed Enhanced Tasmanian Devil Optimization (ETDO) algorithm ensures efficient convergence and robust parameter tuning, aiding its adaptive step size. By validating this framework against expert-provided labels, we demonstrated its clinical relevance and superior performance in segmentation tasks. Our approach reduces dependency on labeled datasets, achieves computational efficiency, and is deployable in real time, making it a compelling alternative for hyperspectral medical image classification and segmentation.

The remainder of this article is structured as follows: The Methodology section outlines the adopted approach, followed by the proposed USSGAN Framework section, which presents the USSGAN model and the Enhanced Tasmanian Devil Optimization (ETDO). The Results section provides the experimental findings, which are further analyzed in the Discussion section, including the ablation studies. Finally, the article concludes with key insights and directions for future research.

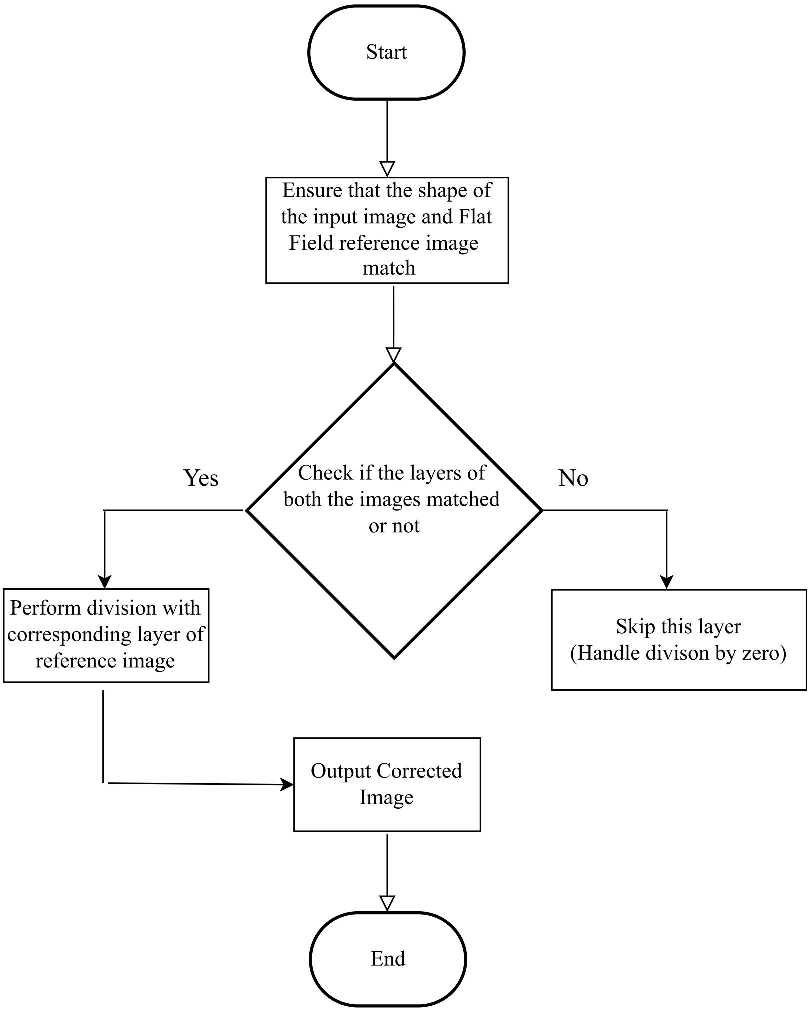

Figure 2. Flowchart for flat field correction.

■ METHODOLOGY

The complete process of classification using USSGAN is shown in Figure 1. Before applying USSGAN, multiple preprocessing steps are implemented, which is referred to as preprocessing chain. These steps are elaborated in the following section.

Designed Preprocessing Pipeline

The preprocessing pipeline for hyperspectral images in this work consists of five major steps, i.e., flat field correction for uniform illumination, Gaussian smoothing for noise reduction, intensity normalization, denoising using Non-Local Means (NLM) algorithm, and band selection by maximum variance[39] with spatial resizing. These steps are applied sequentially to each spectral band of the hyperspectral image, followed by resizing and channel selection using the maximum variance method[39] for further analysis. The details of each step are described in the following sections.

Flat Field Correction. Flatfield correction (FFC) is a crucial preprocessing step applied to this multidimensional choledochal dataset[40,41] to mitigate variable illumination across images. Such variability often arises from factors such as inconsistencies in the light source, optical path, sensor sensitivity, and vignetting. The FFC addresses these issues by dividing the acquired image by a reference flat-field image, typically a blank image without a sample, to compensate for uneven illumination. This process improves the image quality by scaling the data to a uniform range and reducing systematic noise, ultimately facilitating a more accurate analysis. Figure 2 summarizes the process followed to perform the FFC.

Gaussian Smoothing. Hyperspectral images often contain random noise introduced during acquisition,[42] and Gaussian smoothing suppresses this noise in each band, thereby ensuring cleaner data for further processing. Unlike many aggressive denoising techniques, it retains essential spatial structures, making it highly suitable for hyperspectral data, where both spatial and spectral information are equally important. Additionally, by removing unwanted noise, Gaussian smoothing improves the stability and accuracy of subsequent processing tasks, such as segmentation or classification.

The Gaussian smoothing operation is mathematically defined as

$$I_{\text{blurred}}(x, y) = \sum_{i=-k}^{k} \sum_{j=-k}^{k} G(i, j, \sigma) \cdot I(x + i, y + j) \tag{1}$$

where $I(x, y)$ represents the intensity at pixel (x, y) in the spectral band, $G(i, j, \sigma)$ is a Gaussian kernel with a standard deviation σ, and k is the half-width of the kernel.

This formulation ensures that the Gaussian kernel is symmetric around the central pixel (x, y), thereby preserving the spatial alignment. Symmetry allows for uniform smoothing across the image, which is crucial in hyperspectral data processing to maintain the spatial and spectral integrity of the image during denoising.

Min-Max Normalization. After Gaussian smoothing, the intensity values of each band were normalized to the range [0, 255]to standardize the input data. The normalization is defined as

$$I_{\text{norm}}(x, y) = 255 \cdot \frac{I_{\text{blurred}}(x, y) - \min(I_{\text{blurred}}(x, y))}{\max(I_{\text{blurred}}(x, y)) - \min(I_{\text{blurred}}(x, y))} \tag{2}$$

where $\min(I_{\text{blurred}})$ and $\max(I_{\text{blurred}})$ represent the minimum and maximum intensity values in the band, respectively. If $\max(I_{\text{blurred}}) = \min(I_{\text{blurred}})$, the normalized image is set to zero to avoid division by zero.

Non-Local Means (NLM) Denoising. To further suppress noise, the NLM denoising algorithm[43] is applied to each normalized band. NLM estimates each pixel's intensity by averaging similar pixel intensities within a defined search window. The denoised intensity at a pixel is computed as

$$I_{\text{denoised}}(x, y) = \frac{\sum_{p \in W} w(x, y, p) \cdot I_{\text{norm}}(p)}{\sum_{p \in W} w(x, y, p)} \tag{3}$$

where W is the search window, and $w(x, y, p)$ is the weight based on the similarity between the neighborhoods of pixels (x, y) and p. The parameters used were $h = 5$ for filtering strength, a template window size of 3 × 3, and a search window size of 3 × 3.[44] This two-step denoising strategy - comprising Gaussian blur followed by nonlocal means (NLM) denoising - was experimentally found to enhance the quality and consistency of the band inputs used for segmentation and classification, particularly in medical hyperspectral images (HSIs), where signal quality is critical.

Spectral Band Selection and Spatial Resizing. We opted to use the maximum variance technique.[39] This approach involves calculating the variance for all bands and then selecting the two consecutive bands, followed by the band having the maximum variance. Adjacent bands in hyperspectral data are usually correlated and may share complementary information, selecting the bands near the high-variance band. For example, if an image has maximum variance at the 19th band, then its next two consecutive bands, 20th and 21st, can capture related features that enhance classification or segmentation performance.

The selected channels are stacked to reconstruct the hyperspectral cube, which is then resized to a spatial resolution of 128 × 128 from 1024 × 1280 using bilinear interpolation[45] which is mathematically represented as $I_{\text{resized}} = \text{Resize}(I_{\text{stacked}}, 128 \times 128)$

Finally, the bands were selected based on the maximum variance method[39] for further analysis. The resized and normalized image can be represented as

$$I_{\text{final}}(x, y, c) = \frac{I_{\text{resized}}(x, y, c)}{255} \text{where } c \in (\text{selected spectral bands}) \tag{4}$$

This preprocessing pipeline ensures that the hyperspectral data are standardized, denoised, and resized while retaining key spatial and spectral features critical for subsequent processing and analysis.

■ PROPOSED USSGAN FRAMEWORK

In the proposed framework, we combined spatial and spectral attention machines with GANs for hyperspectral image segmentation and classification. GANs achieve classification and segmentation by learning to generate high-quality data representations through the interplay between two models: a generator (G) and a discriminator (D).

Additionally, the proposed framework levarages superpixel-based refinement between G and D models, and Enhanced Tansmanian Devil Optimization (ETDO) for feature map optimization to achieve robust segmentation without relying on lableled data during training. The proposed GAN architecture, its training process, and the proposed enhancement of the existing TDO algorithm are detailed in the subsequent sections.

GAN Architecture and Training

In the GAN architecture, the generator (G) produces segmentation maps directly from the hyperspectral input, whereas the discriminator (D) evaluates these predictions to determine their plausibility. This adversarial setup is formulated as

$$\min_G \max_D \mathbb{E}_{x \sim p_{\text{data}}}[\log D(x)] + \mathbb{E}_{z \sim p_z}[\log(1 - D(G(z)))] \tag{5}$$

where the terms $\mathbb{E}$ denote the expectation values over the data distribution p_{data} and noise distribution p_z. The generator continuously improves its segmentation accuracy by minimizing its loss against the discriminator, whereas the discriminator refines its ability to classify real and generated outputs through adversarial training. Both networks are trained adversarially, with the generator improving its ability to produce plausible segmentations and the discriminator refining its capability to distinguish between real and generated outputs. The generator and discriminator architectures are summarized in Table 1.

Table 1. Summary of the USSGAN Generator and Discriminator Architecture, Detailing the Layer Types and Their Corresponding Output Dimensions

component	layer type	output dimension
generator	input layer	$128 \times 128 \times 3$
	convolutional layers (M layers)	$128 \times 128 \times p$
	spectral spatial attention + softmax	$128 \times 128 \times q$
discriminator	input layers	$128 \times 128 \times 3$, $128 \times 128 \times q$
	convolutional + fusion	$128 \times 128 \times 128$
	dense + sigmoid	1

The proposed GAN architecture in Figure 3 for HSI segmentation and classification integrates a Spatial-Spectral Attention module, generator model, and discriminator model designed to enhance feature extraction and classification.

The generator begins with an input layer of shape (128 × 128 × 3) to process the preprocessed HSI image, followed by a series of convolutional layers repeated M times, each equipped with p filters, a kernel size of (3 × 3) ReLU activation, and the same padding to capture spatial features while maintaining the resolution. Batch normalization is applied after each convolution to stabilize and accelerate training. A custom Spatial-Spectral Attention layer is employed to aggregate spectral information into spatially significant regions by using global

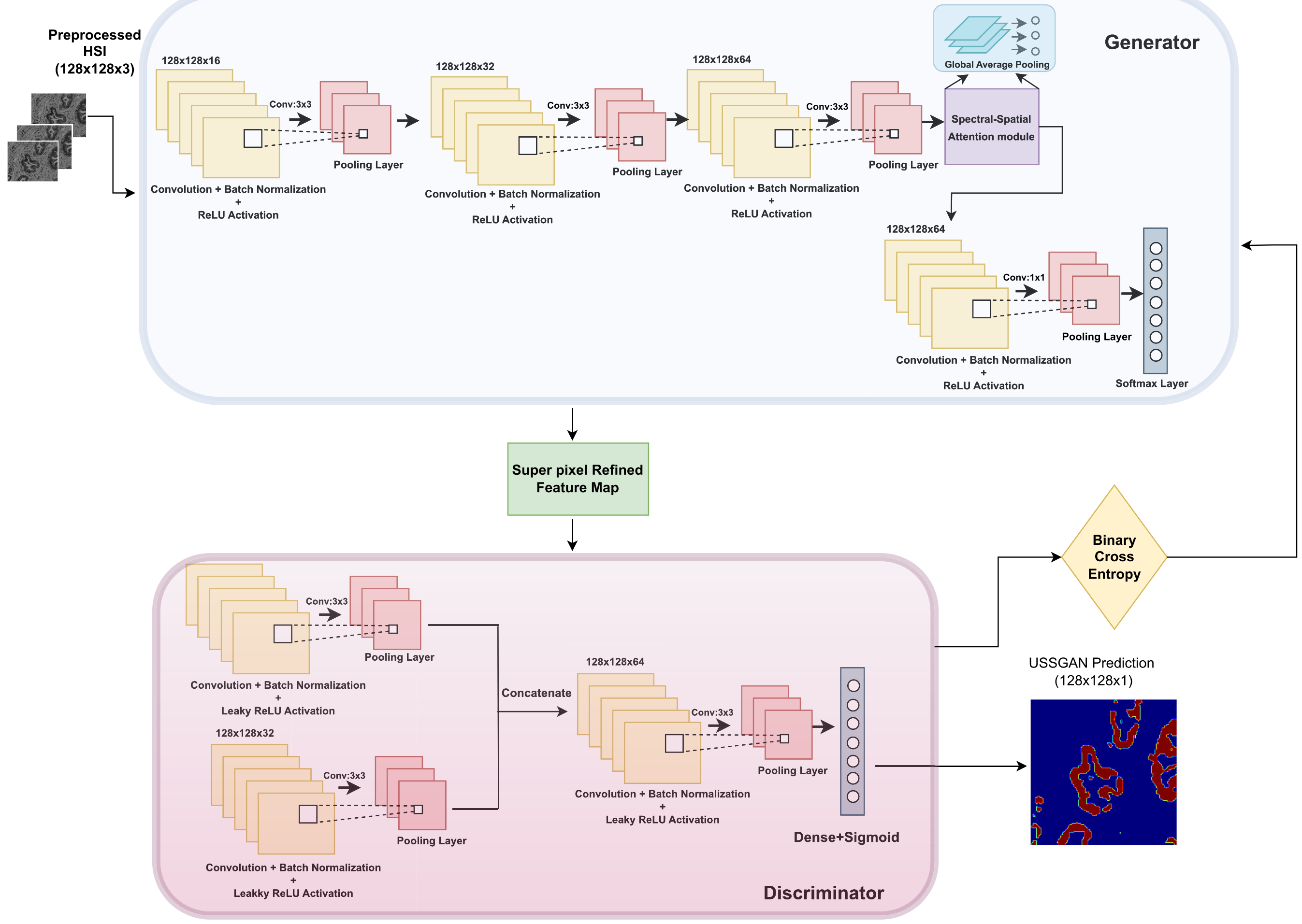

Figure 3. Architecture of the USSGAN framework: Processes input HSI through a generator with spectral-spatial attention for feature enhancement, discriminator for adversarial learning.

average pooling along the spectral dimension, ensuring that critical areas of the image are emphasized. Subsequently, a classification module utilizes a 1 × 1 convolutional layer with q filters to reduce dimensionality, batch normalization to refine feature maps, and a softmax classifier to assign probabilistic pixel-wise class labels.

The discriminator is structured to distinguish between real and generated images. It takes two inputs: the real or generated image of the shape (128 × 128 × 3) and the corresponding prediction of the shape (128 × 128 × 2) from the generator. Both inputs pass through parallel convolutional layers with 64 filters, (3 × 3) kernels, same padding, and LeakyReLU activation (negative slope = 0.2) to avoid issues of dying neurons. Their feature maps were concatenated and processed further through convolutional layers with 128 filters and LeakyReLU activation to extract the combined features. The final output layer was a dense layer with a single unit and sigmoid activation to predict whether the input image was real or generated. The GAN model combines the generator and discriminator, freezing the discriminator weights during the generator training to ensure that the generator improves independently.

Superpixel refinement is employed as a postprocessing step for the generators output, leveraging the jet colormap and RGB conversion for segmentation based on color similarity. Morphological operations, such as closing, are applied to remove small connected components, enhancing spatial coherence in the segmented output. The choice of ReLU activation in the generator encourages sparse feature learning, whereas LeakyReLU in the discriminator prevents vanishing gradients. Batch normalization is consistently used to stabilize training, while softmax in the generator enables probabilistic pixel-wise classification and sigmoid in the discriminator supports binary classification for real versus fake images. This architecture effectively combines spatial and spectral attention with GAN-based learning to enhance hyperspectral image segmentation and classification.

Enhanced Tasmanian Devil Optimization (ETDO)

Tasmanian Devil Optimization (TDO) is a metaheuristic algorithm inspired by the aggressive feeding behavior and social hierarchy of Tasmanian devils.[46] It employs a population-based strategy in which agents representing potential solutions iteratively compete and cooperate within the search space to converge toward the global optimum. The position update of an agent in TDO is mathematically defined as

$$X_i^{t+1} = X_i^t + \alpha \cdot r \cdot (X_{\text{best}} - X_i^t) \tag{6}$$

where X_i^t represents the position of the ith agent at iteration t, α is the step size, r is a random number in $[0, 1]$, and X_{best} denotes the position of the best agent. This balance between exploration and exploitation makes TDO effective for general

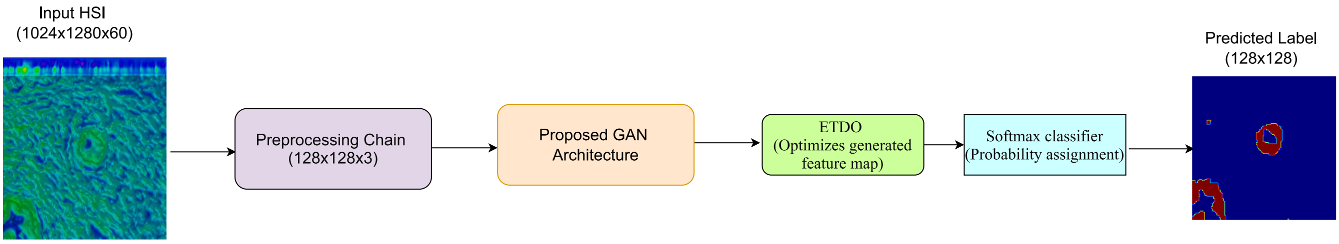

Figure 4. USSGAN Framework: Incorporating ETDO with proposed GAN architecture helps in optimized segmentation results.

optimization problems. However, its performance can be limited when applied to high-dimensional tasks, such as hyperspectral image segmentation, owing to challenges in convergence speed and precision.

To address these limitations, we propose the Enhanced Tasmanian Devil Optimization (ETDO), which introduces three major improvements to the original TDO framework:

1. **Adaptive Step Size:** The step size α is made adaptive and dynamically adjusted throughout the optimization process. This adjustment, governed by an exponential decay function, enables the algorithm to perform broad exploration during early iterations and progressively focus on local refinement as convergence approaches:

$$\alpha = \alpha_{\text{initial}} \cdot \exp(-\beta \cdot t) \tag{7}$$

   where α_{initial} denotes the initial step size, β denotes the decay factor, and t denotes the current iteration.

2. **Local Refinement Mechanism:** ETDO incorporates a local refinement mechanism to enhance the solution precision near promising regions. By introducing small perturbations to the agent's position using a normal distribution, the algorithm effectively refines the solutions in regions close to the global optimum:

$$X_i^{t+1} = X_i^t + \gamma \cdot \text{randn}(0,\ 1) \tag{8}$$

   Here, γ controls the magnitude of the perturbation and randn(0,1) is a random number drawn from a standard normal distribution.

```
Algorithm 1: Enhanced Tasmanian Devil Optimization (ETDO)
Input: Objective function $f$, population size $N$, maximum iterations $T$, initial step
       size $\alpha_{\text{initial}}$, decay factor $\beta$, perturbation factor $\gamma$
Output: Optimal solution $X_{\text{best}}$
Initialize population $\{X_1, X_2, \ldots, X_N\}$ randomly;
Evaluate the fitness of each agent: $F_i = f(X_i)$, where $i = 1, 2, \ldots, N$;
Identify the best solution: $X_{\text{best}} = \arg\min_i F_i$;
for each iteration $t = 1, 2, \ldots, T$ do
    Update step size: $\alpha = \alpha_{\text{initial}} \cdot \exp(-\beta \cdot t)$;
    for each agent $i = 1, 2, \ldots, N$ do
        Update position: $X_i^{t+1} = X_i^t + \alpha \cdot r \cdot (X_{\text{best}} - X_i^t)$, where $r \sim U(0,1)$;
        Apply local refinement: $X_i^{t+1} = X_i^{t+1} + \gamma \cdot \text{randn}(0,1)$;
        Evaluate new fitness: $F_i = f(X_i^{t+1})$;
    Update $X_{\text{best}} = \arg\min_i F_i$ based on fitness values;
return $X_{\text{best}}$;
```

3. **Weighted Fitness Function:** ETDO utilizes a weighted fitness function to prioritize solutions that balance spatial and spectral features. This refinement directly addresses the unique challenges of hyperspectral image segmentation, in which both spectral accuracy and spatial coherence are critical for generating clinically meaningful segmentation maps.

These enhancements significantly improve the convergence speed, solution precision, and ability to navigate the high-

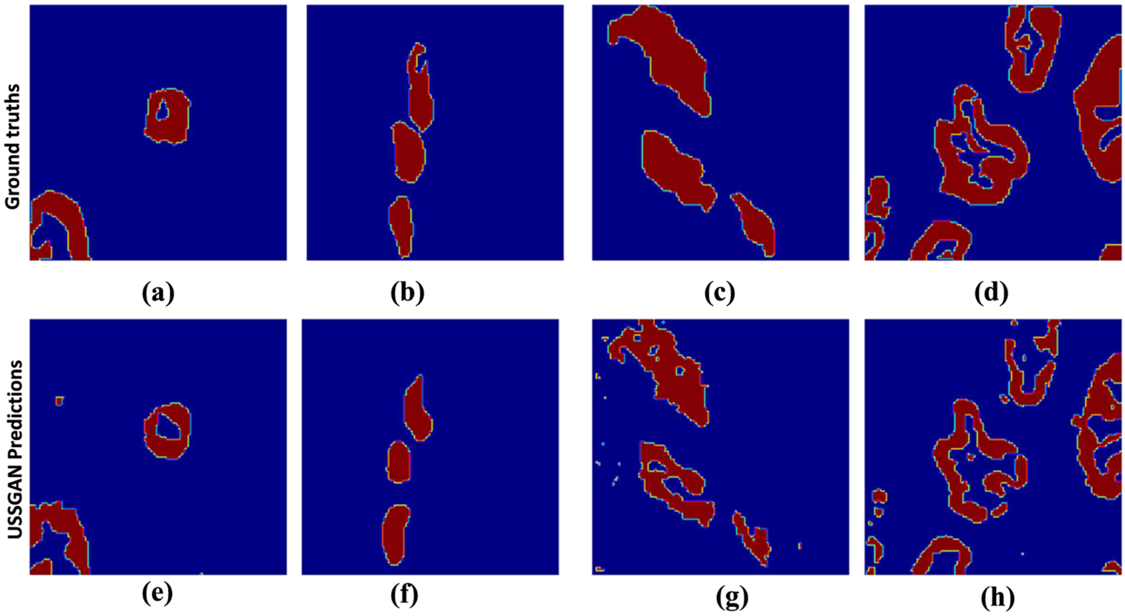

Figure 5. Top row (a−d) Ground Truths: tumor region in red and background in blue. These annotations served as the benchmark for evaluating the segmentation performance. The bottom row (e−h) presents the corresponding predictions generated by the proposed USSGAN. The results demonstrate the model's ability to accurately segment tumor regions with minimal discrepancy from the ground truth, Subtle differences in predictions (e.g., at the edges) highlight the challenges in unsupervised segmentation and areas for further refinement.

dimensional search space of hyperspectral data, enabling ETDO to effectively optimize segmentation parameters, as shown in Figure 4. The proposed ETDO can be summarized using the following Algorithm 1. The algorithm operates on a population of agents, each representing a candidate solution, and iteratively improves these solutions to converge toward an optimal outcome. Initially, the population of agents $\{X_1, X_2, ..., X_N\}$ is randomly initialized, and their fitness values are evaluated using the objective function $f(X)$, which quantifies the quality of each solution. The best-performing agent, X_{best}, is identified as the one minimizing the fitness value.

The optimization process proceeds over T iterations. During each iteration, an adaptive step size

$$\alpha = \alpha_{\text{initial}} \cdot \exp(-\beta \cdot t)$$

where α_{initial} is the initial step size, β is the decay factor that controls the rate of reduction, and t is the current iteration.

Each agent i updates its position using the following formula:

$$X_i^{t+1} = X_i^t + \alpha \cdot r \cdot (X_{\text{best}} - X_i^t)$$

where $r \sim U(0, 1)$ denotes a random scalar that ensures the stochasticity. Additionally, local refinement is applied

$$X_i^{t+1} = X_i^{t+1} + \gamma \cdot \text{randn}(0, 1)$$

where γ controls the magnitude of the perturbation and $\text{randn}(0, 1)$ is a random value drawn from a standard normal distribution. This refinement step enhances the solution precision.

At the end of each iteration, the fitness of all agents is re-evaluated, and the global best X_{best} is updated if a better solution is found. After T iterations, the algorithm outputs an optimal solution, X_{best}. The proposed framework incorporates proposed GAN architecture in Figure 3 with ETDO and the entire frameworks is depicted as Figure 4

■ RESULTS AND DISCUSSION

Dataset Description

In this section, we discuss the results obtained from the proposed methodology. For our experimental analysis, we utilized publicly available multidimensional choledochal data sets of cholangiocarcinoma,[40] comprising 888 scenes collected from 174 individuals. The dataset entry ”030406−20x-roi1” follows the format patient registration id-microscope magnification level-region of interest. Further details regarding the dataset can be found in ref 40.

Model Performance and Comparative Analysis with State of the Art (SOTA)

Figure 5 compares the ground-truth annotations by pathologists (Figure 5a−d) with the predictions from the proposed USSGAN model (Figure 5e−h). The USSGAN effectively captures the boundaries and intricate structures of pathological regions in an unsupervised manner, aligning closely with the ground truth. The spatial attention mechanism within the USSGAN demonstrates robust performance by reducing noise and ensuring accurate delineation, especially in smaller regions. The predictions reflect high fidelity and spatial consistency, highlighting the model’s ability to address the challenges of hyperspectral image segmentation. The performance of our proposed USSGAN model is validated across various subjects in the dataset using metrics such as Overall Accuracy (OA), Average Accuracy (AA), and Cohens Kappa. These quantitative results are shown in Table 2.

Table 2. Classification Metrics for the Input HSI’s are Evaluated using OA, AA, and Cohen’s Kappa[a]

input HSI	OA (%)	AA (%)	Cohen’s Kappa (%)
032236−20x-roi4	98.03	85.53	83.44
033629_3−20x-roi5	97.10	77.63	72.12
031368−20x-roi3	96.00	84.88	82.95
031368c-20x-roi2	90.63	76.13	71.82

[a] The table provides the performance metrics for the four different input HSI datasets. Higher values indicate better model performance. The results highlight the variation in classification performance across different subjects from the dataset.

Figure 6 compares the segmentation performance of the proposed USSGAN with a wide range of traditional ML, DL, and transformer-based models, including SVM, DNN,[40] 3D U-Net,[17] convolutional autoencoder,[47] DeepLabV3++,[48] attention-based 2D U-Net,[49] Vision Transformer[50] and some recent studies like MRANET,[19] MAEFNET,[21] and HCLA-U-NET.[20] SVM, often fall short in hyperspectral segmentation tasks. Among these, SVM achieves moderate accuracy but lacks spatial context awareness, limiting its robustness. Supervised deep learning methods, such as DNN and 3D U-Net, show notable improvement in capturing tumor regions. However, DNN misses fine spatial structures, and 3D U-Net occasionally struggles with boundary precision. The convolutional autoencoder performs better than shallow models but still lags behind modern segmentation networks in spatial coherence. More advanced architectures like DeepLabV3+ and Vision Transformer offer higher accuracy, benefiting from multiscale context aggregation and global attention mechanisms. HCLA U Net achieves the highest AA (91.16.%) and a strong Cohen’s Kappa score (79.42%), while Vision Transformer performs competitively in terms of OA (94.14%) and Cohen’s Kappa (83.01%). However, both still show minor limitations in preserving edge details. Recently introduced DL models such as MAEFNet[21] and MRANet[19] demonstrate superior performance due to attention-guided learning and multiresolution fusion mechanisms. MAEFNet achieves competitive AA (87.71%) and Cohen’s Kappa (80.86%), highlighting its ability to capture boundary details with contextual focus. MRANet shows balanced performance (OA = 89.40%, AA = 89.74%) and excels in spatial refinement through multipath attention. The HCLA U-Net[20] further improves boundary delineation by incorporating hierarchical channel-level attention, resulting in the highest AA (91.16%) among all methods and a strong Cohen’s Kappa score (82.75%). In contrast, the proposed USSGAN outperforms all other methods with the highest Overall Accuracy (98.03%), competitive Average Accuracy (85.53%), and the best Cohens Kappa score (83.44%), indicating superior agreement with ground truth annotations. USSGAN achieves this by integrating unsupervised spatial attention with spectral encoding, resulting in precise segmentation with minimal noise. The results corresponding to Figure 6 are quantified in Table 3.

Ablation Study

The ablation study evaluates the impact of key components in the USSGAN framework, specifically enhanced Tasmanian

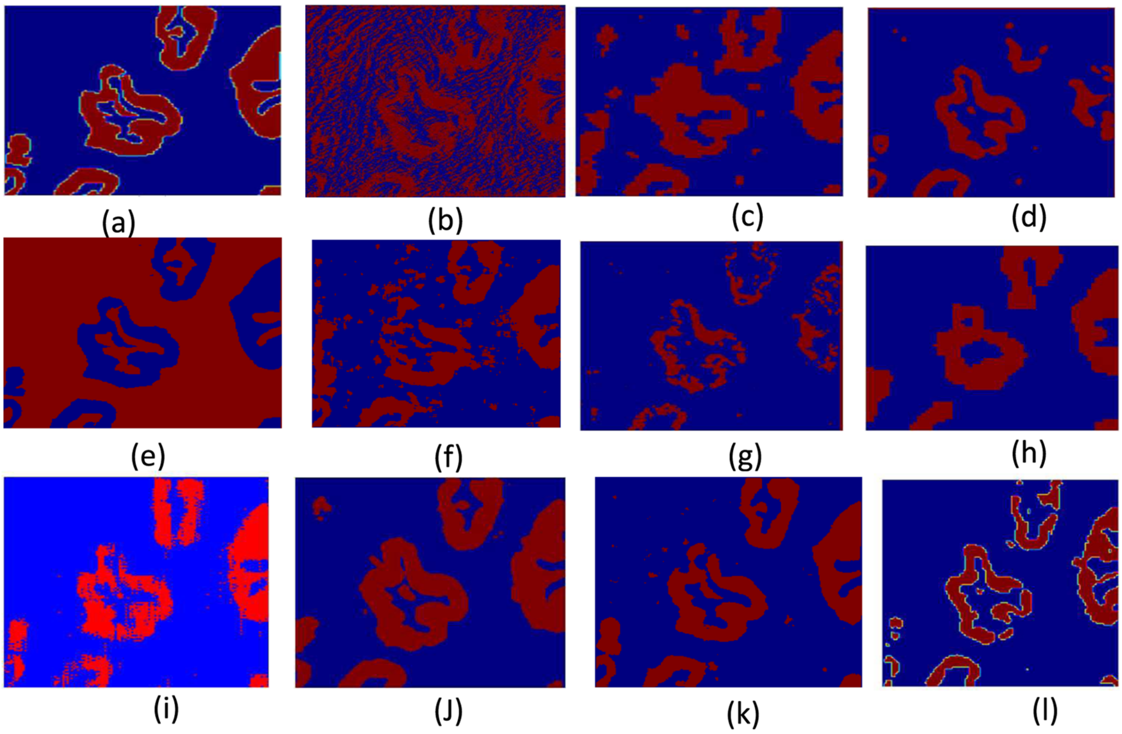

Figure 6. Qualitative ground truth comparison with various Traditional and state-of-the-art models. (a) Ground Truth (GT): Expert-annotated tumor regions. (b) Attention 2D U-NET: Slightly lower spatial consistency, poor boundary preservation, and noisy. (c) Convolutional Autoencoder: Low-level features detected; suffers from oversmoothing. (d) SVM: Moderate boundary precision, but lacks robustness. (e) MAEFNet: Effective boundary refinement with strong attention-driven contextual learning. (f) MRANet: Robust spatial enhancement using multipath residual attention, suitable for small datasets. (g) DNN: Improved detection, but missed finer spatial details. (h) DeepLabV3+: High accuracy with better boundary adherence and region integrity. (i) Vision Transformer: Excellent regional coherence but minor edge misclassifications. (j) 3D U-NET: Accurate, but fails to capture some boundaries. (k) HCLA U-Net: Incorporates channel-level attention into U-Net to improve tumor boundary delineation. (l) **USSGAN (Proposed):** Achieves precise segmentation with minimal noise, demonstrating its superior performance over other methods.

Table 3. Classification Metrics for Various Methods Such as Overall Accuracy (OA), Average Accuracy (AA), and Cohen's Kappa Evaluated on the Dataset[a]

method	OA (%)	AA (%)	Cohen's Kappa (%)
Attention 2D U-Net[49]	49.32	48.54	21.30
convolutional autoencoder[47]	61.66	52.78	50.65
SVM[40]	87.62	68.65	41.97
MAEFNet[21]	88.47	87.71	80.86
MRANet[19]	89.40	89.74	73.10
DNN[40]	91.59	71.39	51.35
DeepLabV3+[48]	92.33	90.25	79.42
vision transformer[50]	94.14	89.55	83.01
3D U-Net[17]	94.49	86.02	75.19
HCLA U-Net[20]	95.72	**91.16**	82.75
USSGAN (proposed)	**98.03**	85.53	**83.44**

[a] The highest values for each metric are highlighted in bold.

Devil Optimization (ETDO) and attention mechanisms, on hyperspectral image segmentation performance. The integration of ETDO improves the precision of segmentation by enabling efficient convergence through an adaptive step size and precise boundary delineation through local refinements. These features are critical for hyperspectral data, where capturing the interplay between spatial and spectral patterns is essential. Validation experiments demonstrate that ETDO-driven optimization leads to significant enhancements. To validate our performed experiments we have chosen the segmentation metrics like sensitivity, specificity, intersection over union (IoU), and dice coefficient along with the overall accuracy to demonstrate the model's holistic capability in terms of classification and segmentation metrics. As summarized in Figure 7 and Table 4, this study highlights the contributions of each module, underscoring their roles in achieving robust and accurate segmentation.

■ DISCUSSION

The results obtained from the ablation experiments are shown in Figure 7 and quantified using Table 4 demonstrating that the combination of ETDO and attention mechanisms in the proposed method achieves the best overall performance across all metrics. This result underscores its superiority in hyperspectral image ETDO, which enhances the sensitivity and IoU by effectively capturing fine boundaries and accurately identifying positive regions. Attention mechanisms, however, improve specificity, reduce false positives, and refine the segmentation of key regions. The synergy between the two is evident, as combining these techniques balances sensitivity and specificity, achieving the highest IoU and Dice coefficients and ensuring both comprehensive coverage of true positive regions and precise segmentation.

Interestingly, the impact of these enhancements varied across the datasets. For Patient 1 (032236−20x-roi4), ETDO provided significant gains in sensitivity and IoU, highlighting its importance in detecting challenging boundaries. In contrast, for Patient 2 (033629_3−20x-roi5), the attention module

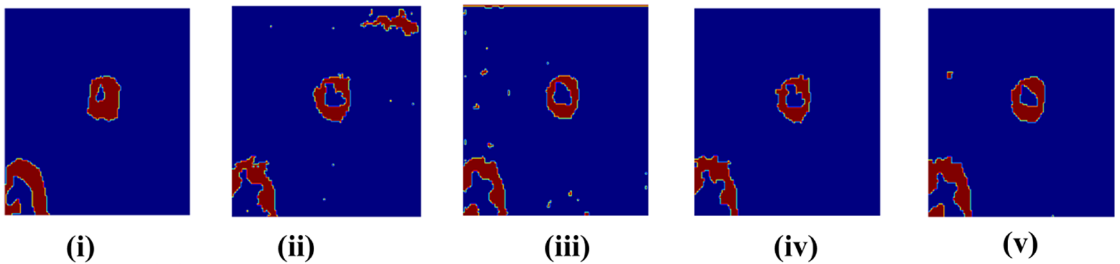
(i) (ii) (iii) (iv) (v)

(a) Ablation studies on patient ID: 032236-20x-roi4.

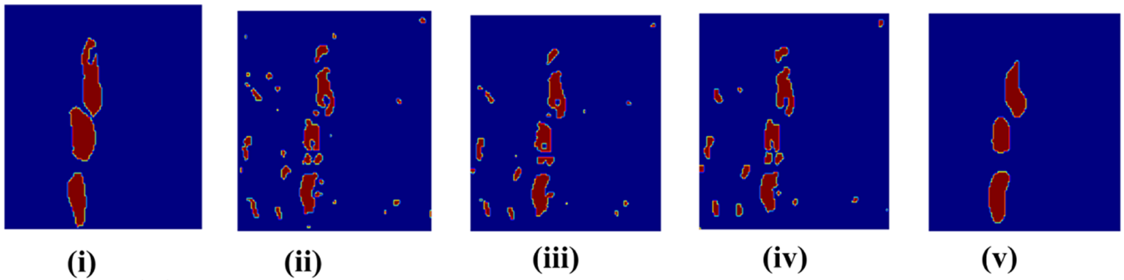
(i) (ii) (iii) (iv) (v)

(b) Ablation studies on patient ID: 033629_3-20x-roi5.

Figure 7. For Figures (a) and (b): (i) Ground truth, (ii) without proposed enhancements, (iii) without spectral-spatial attention module, (iv) without proposed enhancement in TDO (v) with proposed enhancements.

Table 4. Segmentation Metrics for Various Ablation Studies on Two Subjects[a]

input HSI	use cases	OA (%)	sensitivity (%)	specificity (%)	IoU (%)	dice (%)
032236−20x-roi4	with basic GAN	95.18	71.72	97.64	53.42	69.64
	GAN+ETDO	97.49	83.20	98.67	69.76	82.19
	GAN+ SSA (spectral spatial attention)	96.72	70.49	99.15	62.75	77.11
	USSGAN (proposed)	**98.03**	**83.20**	**99.05**	**73.14**	**84.48**
033629_3−20x-roi5	with basic GAN	93.48	74.83	96.76	62.95	77.26
	GAN+ETDO	94.94	79.21	98.47	72.72	84.20
	GAN+ SSA (spectral spatial attention)	95.48	78.83	98.94	74.28	85.24
	USSGAN (proposed)	**97.10**	**85.38**	**99.12**	**83.26**	**89.92**

[a] The proposed method (maintaining both the attention module and TDO enhancements) consistently achieved the highest performance across all metrics, demonstrating its effectiveness. For both HSI inputs, removing the attention module or TDO enhancements results in significant drops in IoU and Dice scores, highlighting the critical contribution of these components.

showed a larger impact, achieving notable improvements in specificity and region refinement. This variability suggests that each enhancement addresses different segmentation challenges, and their combined use leverages their strengths to achieve the best results. This observation reinforces the idea that neither ETDO nor the attention module alone is sufficient to consistently achieve optimal performance across diverse datasets. Instead, their complementary nature ensures robust and precise segmentation, which is critical for medical applications in which both under- and oversegmentation carry significant risks. Integrating ETDO helped us achieve a slightly faster convergence of the model. Although we have not detailed the analysis of computational complexity, the base model itself is capable of achieving convergence at a decent pace.

Experimental Settings and Hyperparameter Tuning

To ensure optimal performance, various parameters were tested during the preprocessing and training of the USSGAN framework. In the preprocessing stage, a Gaussian kernel of size 3 × 3 was selected after experimenting with various kernel sizes, and the sigma value was set to five based on experimental trials. For the regularization parameter λ, values ranging from 0 to 0.1 were evaluated, with $\lambda = 0.01$ producing the best results reported in this study. For consistency, these preprocessing and hyperparameter settings were kept constant across all the experiments. All experiments with USSGAN were conducted on a personal computer equipped with 8 GB of RAM, an AMD Ryzen 5 processor with integrated graphics, and a clock speed of 2.10 GHz. Remarkably, despite the modest hardware configuration, the model was able to generate results in less than a minute, demonstrating its computational throughput and suitability for real-time applications. In contrast, supervised comparative models, including 3D U-Net and other state-of-the-art architectures, were run on a high-performance computing workstation as they need excessive training with an Intel Xeon processor, 32 GB of RAM, a 3.2 GHz clock speed, and a dedicated NVIDIA GTX 1650 GPU. These models require significantly more computational resources to achieve their results.

The ability of USSGAN to deliver comparable or superior segmentation and classification outcomes while operating on a lightweight system highlights its computational throughput and makes it a practical choice for real-world deployment, particularly in resource-constrained environments.

CONCLUSIONS

In this study, we proposed an Unsupervised Spatial Attention-Based Generative Adversarial Network (USSGAN) framework for segmenting hyperspectral images of cholangiocarcinoma tissues. Extensive experimental results demonstrated that USSGAN outperformed traditional machine learning techniques, such as SVM and DNN, as well as state-of-the-art deep learning models, Table 3 specifically, USSGAN achieved an impressive Overall Accuracy (OA) of 98.03%, Average Accuracy (AA) of 85.53%, and Cohens Kappa of 83.44% across diverse hyperspectral image datasets of different patients. Ablation studies revealed the critical impact of individual components within USSGAN, such as the spectral-spatial module and Enhanced Tasmanian Devil Optimization (ETDO). These components significantly contributed to performance improvements by enhancing the spectral-spatial feature extraction and convergence efficiency. The spectral-spatial module demonstrated its capability in capturing intricate dependencies, whereas ETDO ensured better parameter optimization for robust segmentation results. This validates the effectiveness of integrating these modules into the USSGAN framework. The inclusion of spatial attention mechanisms further bolstered the models ability to capture fine-grained details in complex tissue structures, resulting in segmentation maps closely aligned with pathologist-provided ground truths. Importantly, the unsupervised nature of USSGAN eliminates reliance on extensive manual annotations, making it particularly valuable for large-scale biomedical applications in scenarios with limited labeled data. Looking forward, we plan to extend the USSGAN framework to a more generalized model capable of segmenting hyperspectral images across multiple publicly available cancer datasets. This will validate the robustness, scalability, and versatility of the USSGAN in real-world clinical scenarios, ultimately bridging the gap between research advancements and clinical deployment. Our future efforts will also include integrating cross-domain transfer learning techniques to enhance the models adaptability to diverse cancer types and further automate the diagnostic workflow.

AUTHOR INFORMATION

Corresponding Authors

Anuj Deshpande – *Electronics and Communication Department, SRM University-AP, Mangalagiri, Andhra Pradesh 522240, India;* orcid.org/0000-0002-7415-1691; Email: deshpande.a@srmap.edu.in

Hala Mostafa – *Department of Information Technology, College of Computer and Information Sciences, Princess Nourah bint Abdulrahman University, Riyadh 11671, Saudi Arabia*; Email: hfmostafa@pnu.edu.sa

Authors

Sikhakolli Sravan Kumar – *Electronics and Communication Department, SRM University-AP, Mangalagiri, Andhra Pradesh 522240, India;* orcid.org/0000-0002-4887-997X

Pooja A. Nair – *Electronics and Communication Department, SRM University-AP, Mangalagiri, Andhra Pradesh 522240, India;* orcid.org/0000-0002-1937-0509

Suresh Aala – *Electronics and Communication Department, SRM University-AP, Mangalagiri, Andhra Pradesh 522240, India*

Sunil Chinnadurai – *Electronics and Communication Department, SRM University-AP, Mangalagiri, Andhra Pradesh 522240, India*

Vineela Chandra Dodda – *Department of Electronics and Communication Engineering, Amrita School of Engineering Amaravati, Amrita Vishwa Vidyapeetham, Guntur, Andhra Pradesh 522503, India;* orcid.org/0000-0001-7324-2949

Inbarasan Muniraj – *Department of Electronic Engineering, Maynooth University, Maynooth, Co. Kildare W23 V5XH, Ireland*

Md. Abdul Latif Sarker – *Department of Electronics and Information Engineering, Jeonbuk National University, Jeonju 54896, Korea*

Complete contact information is available at: https://pubs.acs.org/10.1021/cbmi.5c00054

Author Contributions

CREDIT: S.S.K., H.M., and A.D. planned the project; V.C.D., S.A., and P.A.N. contributed to simulations; I.M., S.C., and M.L.A.S. mentored the project; all authors discussed the results and contributed equally to manuscript preparation.

Notes

The authors declare no competing financial interest.

ACKNOWLEDGMENTS

The authors acknowledge Princess Nourah Bint Abdulrahman University Researchers Supporting Project number (PNURSP2025R137), Princess Nourah bint Abdulrahman University, Riyadh, Saudi Arabia. The authors also thank Prof. Qingli Li and their research group at East China Normal University, Shanghai, China, for providing access to their dataset

ADDITIONAL NOTE

[†]Unsupervised Cholangiocarcinoma detection

REFERENCES

(1) Society, A. C. Bile Duct Cancer Survival Rates 2022 https://www.cancer.org/cancer/types/bile-duct-cancer/detection-diagnosis-staging/survival-by-stage.html; Last accessed on Jan 29, 2025.

(2) Banales, J. M.; Marin, J. J.; Lamarca, A.; Rodrigues, P. M.; Khan, S. A.; Roberts, L. R.; Cardinale, V.; Carpino, G.; Andersen, J. B.; Braconi, C.; et al. Cholangiocarcinoma 2020: the next horizon in mechanisms and management. *Nat. Rev. Gastroenterol. Hepatol.* **2020**, *17*, 557–588.

(3) Florio, A. A.; Ferlay, J.; Znaor, A.; Ruggieri, D.; Alvarez, C. S.; Laversanne, M.; Bray, F.; McGlynn, K. A.; Petrick, J. L. Global trends in intrahepatic and extrahepatic cholangiocarcinoma incidence from 1993 to 2012. *Cancer* **2020**, *126*, 2666–2678.

(4) Qin, X.-L.; Wang, Z.-R.; Shi, J.-S.; Lu, M.; Wang, L.; He, Q.-R. Utility of serum CA19–9 in diagnosis of cholangiocarcinoma: in comparison with CEA. *World J. Gastroenterol.* **2004**, *10*, 427.

(5) Antequera, T.; Caballero, D.; Grassi, S.; Uttaro, B.; Perez-Palacios, T. Evaluation of fresh meat quality by hyperspectral imaging (HSI), nuclear magnetic resonance (NMR) and magnetic resonance imaging (MRI): a review. *Meat Sci.* **2021**, *172*, No. 108340.

(6) Ponnoprat, D.; Inkeaw, P.; Chaijaruwanich, J.; Traisathit, P.; Sripan, P.; Inmutto, N.; Na Chiangmai, W.; Pongnikorn, D.; Chitapanarux, I. Classification of hepatocellular carcinoma and intrahepatic cholangiocarcinoma based on multi-phase CT scans. *Med. Biol. Eng. Comput.* **2020**, *58*, 2497–2515.

(7) Zhang, T.; Xiang, Y.; Wang, H.; Yun, H.; Liu, Y.; Wang, X.; Zhang, H. Radiomics combined with multiple machine learning algorithms in differentiating pancreatic ductal adenocarcinoma from

pancreatic neuroendocrine tumor: more hands produce a stronger flame. *J. Clin. Med.* **2022**, *11*, 6789.

(8) Sikhakolli, S. K.; Muniraj, I. Hyperspectral imaging and its applications: An Overview. *Asian J. Phys.* **2022**, *31*, 985−998.

(9) He, Z.; Liu, H.; Wang, Y.; Hu, J. Generative adversarial networks-based semi-supervised learning for hyperspectral image classification. *Remote Sens.* **2017**, *9*, 1042.

(10) Li, S.; Song, W.; Fang, L.; Chen, Y.; Ghamisi, P.; Benediktsson, J. A. Deep learning for hyperspectral image classification: An overview. *IEEE Trans. Geosci. Remote Sens.* **2019**, *57*, 6690−6709.

(11) Sawant, S. S.; Prabukumar, M. A review on graph-based semi-supervised learning methods for hyperspectral image classification. *Egypt. J. Remote Sens. Space Sci.* **2020**, *23*, 243−248.

(12) Ge, H.; Pan, H.; Wang, L.; Li, C.; Liu, Y.; Zhu, W.; Teng, Y. A semi-supervised learning method for hyperspectral imagery based on self-training and local-based affinity propagation. *Int. J. Remote Sens.* **2021**, *42*, 6391−6416.

(13) Chen, J.; Sun, B.; Wang, L.; Fang, B.; Chang, Y.; Li, Y.; Zhang, J.; Lyu, X.; Chen, G. Semi-supervised semantic segmentation framework with pseudo supervisions for land-use/land-cover mapping in coastal areas. *Int. J. Appl. Earth Obs. Geoinformation* **2022**, *112*, 102881.

(14) Manian, V.; Alfaro-Mejía, E.; Tokars, R. P. Hyperspectral image labeling and classification using an ensemble semi-supervised machine learning approach. *Sensors* **2022**, *22*, 1623.

(15) Peng, J.; Zhou, Y.; Chen, C. P. Region-kernel-based support vector machines for hyperspectral image classification. *IEEE Trans. Geosci. Remote Sens.* **2015**, *53*, 4810−4824.

(16) Qian, Y.; Ye, M.; Zhou, J. Hyperspectral image classification based on structured sparse logistic regression and three-dimensional wavelet texture features. *IEEE Trans. Geosci. Remote Sens.* **2013**, *51*, 2276−2291.

(17) Kumar, S. S.; Sahoo, O. P.; Mundada, G.; Aala, S.; Sudarsa, D.; Pandey, O. J.; Chinnadurai, S.; Matoba, O.; Muniraj, I.; Deshpande, A. Deep learning-based hyperspectral microscopic imaging for cholangiocarcinoma detection and classification. *Opt. Continuum* **2024**, *3*, 1311−1324.

(18) Zhang, Y.; Dong, J. SAHIS-Net: a spectral attention and feature enhancement network for microscopic hyperspectral cholangiocarcinoma image segmentation. Biomedical. *Opt. Express* **2024**, *15*, 3147−3162.

(19) Wahid, A.; Mahmood, T.; Hong, J. S.; Kim, S. G.; Ullah, N.; Akram, R.; Park, K. R. Multi-path residual attention network for cancer diagnosis robust to a small number of training data of microscopic hyperspectral pathological images. *Eng. Appl. Artif. Intell.* **2024**, *133*, No. 108288.

(20) Gao, H.; Yang, M.; Cao, X.; Liu, Q.; Xu, P. A high-level feature channel attention UNet network for cholangiocarcinoma segmentation from microscopy hyperspectral images. *Mach. Vision Appl.* **2023**, *34*, No. 72.

(21) Zhang, Y.; Dong, J. Maef-net: Mlp attention for feature enhancement in u-net based medical image segmentation networks. *IEEE J. Biomed. Health Inf.* **2024**, *28*, 846−857.

(22) Chakrabarti, S.; Rao, U. S. Lightweight neural network for smart diagnosis of cholangiocarcinoma using histopathological images. *Sci. Rep.* **2023**, *13*, No. 18854.

(23) Wang, Z.; Tang, H. Artificial Intelligence for Quantum Error Correction: A Comprehensive Review. arXiv:2412.20380. arXiv.org e-Print archive. https://arxiv.org/abs/2412.20380; 2024.

(24) Gui, J.; Wang, S.-L.; Lei, Y.-K. Multi-step dimensionality reduction and semi-supervised graph-based tumor classification using gene expression data. *Artif. Intell. Med.* **2010**, *50*, 181−191.

(25) Xu, Y.-Y.; Yang, F.; Zhang, Y.; Shen, H.-B. Bioimaging-based detection of mislocalized proteins in human cancers by semi-supervised learning. *Bioinformatics* **2015**, *31*, 1111−1119.

(26) Thul, P. J.; Lindskog, C. The human protein atlas: a spatial map of the human proteome. *Protein Sci.* **2018**, *27*, 233−244.

(27) Ma, T.; Zhang, A. Affinity network fusion and semi-supervised learning for cancer patient clustering. *Methods* **2018**, *145*, 16−24.

(28) Kumar, N.; Uppala, P.; Duddu, K.; Sreedhar, H.; Varma, V.; Guzman, G.; Walsh, M.; Sethi, A. Hyperspectral tissue image segmentation using semi-supervised NMF and hierarchical clustering. *IEEE Trans. Med. Imaging* **2019**, *38*, 1304−1313.

(29) Sikhakolli, S. K.; Aala, S.; Chinnadurai, S.; Muniraj, I.; Deshpande, A. Cholangiocarcinoma Classification Using Semi-Supervised Learning Approach. 3D Image Acquisition and Display: Technology. *Percept. Appl.* **2024**, DW3H−3.

(30) Halicek, M.; Lu, G.; Little, J. V.; Wang, X.; Patel, M.; Griffith, C. C.; El-Deiry, M. W.; Chen, A. Y.; Fei, B. Deep convolutional neural networks for classifying head and neck cancer using hyperspectral imaging. *J. Biomed. Opt.* **2017**, *22*, No. 060503.

(31) Wang, Q.; Sun, L.; Wang, Y.; Zhou, M.; Hu, M.; Chen, J.; Wen, Y.; Li, Q. Identification of melanoma from hyperspectral pathology image using 3D convolutional networks. *IEEE Trans. Med. Imaging* **2021**, *40*, 218−227.

(32) Wei, X.; Li, W.; Zhang, M.; Li, Q. Medical hyperspectral image classification based on end-to-end fusion deep neural network. *IEEE Trans. Instrum. Meas.* **2019**, *68*, 4481−4492.

(33) Zeng, W.; Li, W.; Zhang, M.; Wang, H.; Lv, M.; Yang, Y.; Tao, R. Microscopic hyperspectral image classification based on fusion transformer with parallel cnn. *IEEE J. Biomed. Health Inform.* **2023**, *27*, 2910−2921.

(34) Muhammad, H.; Sigel, C. S.; Campanella, G.; Boerner, T.; Pak, L. M.; Büttner, S.; IJzermans, J. N.; Koerkamp, B. G.; Doukas, M.; Jarnagin, W. R.et al.Unsupervised subtyping of cholangiocarcinoma using a deep clustering convolutional autoencoder. In *Medical Image Computing and Computer Assisted Intervention−MICCAI 2019:22nd International Conference, Shenzhen, China, October 13−17, 2019, Proceedings, Part I 22* 2019; pp 604−612.

(35) Wang, M.; Xu, Y.; Wang, Z.; Xing, C. Deep margin cosine autoencoder based medical hyperspectral image classification for tumor diagnosis. *IEEE Trans. Instrum. Meas.* **2023**, *72*, 1−12, DOI: 10.1109/TIM.2023.3293548.

(36) Goodfellow, I.; Pouget-Abadie, J.; Mirza, M.; Xu, B.; Warde-Farley, D.; Ozair, S.; Courville, A.; Bengio, Y. Generative adversarial networks. *Commun. ACM* **2020**, *63*, 139−144.

(37) Utkarsh; Jain, P. K. Predicting bentonite swelling pressure: optimized XGBoost versus neural networks. *Sci. Rep.* **2024**, *14*, No. 17533.

(38) Zhu, L.; Chen, Y.; Ghamisi, P.; Benediktsson, J. A. Generative adversarial networks for hyperspectral image classification. *IEEE Trans. Geosci. Remote Sens.* **2018**, *56*, 5046−5063.

(39) Siddiqa, A.; Islam, R.; Afjal, M. I. Spectral segmentation based dimension reduction for hyperspectral image classification. *J. Spat. Sci.* **2023**, *68*, 543−562.

(40) Zhang, Q.; Li, Q.; Yu, G.; Sun, L.; Zhou, M.; Chu, J. A multidimensional choledoch database and benchmarks for cholangiocarcinoma diagnosis. *IEEE Access* **2019**, *7*, 149414−149421.

(41) Wang, Y.; Gu, Y.; Li, X. A Novel Low Rank Smooth Flat-Field Correction Algorithm for Hyperspectral Microscopy Imaging. *IEEE Trans. Med. Imaging* **2022**, *41*, 3862−3872.

(42) Gao, L.; Smith, R. T. Optical hyperspectral imaging in microscopy and spectroscopy-a review of data acquisition. *J. Biophotonics* **2015**, *8*, 441−456.

(43) Tu, B.; Zhang, X.; Wang, J.; Zhang, G.; Ou, X. Spectral-spatial hyperspectral image classification via non-local means filtering feature extraction. *Sens. Imaging* **2018**, *19*, 1−25.

(44) Maeda, Y.; Fukushima, N.; Matsuo, H. Effective implementation of edge-preserving filtering on cpu microarchitectures. *Appl. Sci.* **2018**, *8*, 1985.

(45) Ying, J.; Shen, H.-L.; Cao, S.-Y. Unaligned hyperspectral image fusion via registration and interpolation modeling. *IEEE Trans. Geosci. Remote Sens.* **2022**, *60*, 1−14.

(46) Dehghani, M.; Hubálovský, Š.; Trojovský, P. Tasmanian devil optimization: a new bio-inspired optimization algorithm for solving optimization algorithm. *IEEE Access* **2022**, *10*, 19599−19620.

(47) Nalepa, J.; Myller, M.; Imai, Y.; Honda, K.-i.; Takeda, T.; Antoniak, M. Unsupervised segmentation of hyperspectral images

using 3-D convolutional autoencoders. *IEEE Geosci. Remote Sens. Lett.* **2020**, *17*, 1948−1952.

(48) Wang, Y.; Yang, L.; Liu, X.; Yan, P. An improved semantic segmentation algorithm for high-resolution remote sensing images based on DeepLabv3. *Sci. Rep.* **2024**, *14*, No. 9716.

(49) Noori, M.; Bahri, A.; Mohammadi, K.Attention-guided version of 2D UNet for automatic brain tumor segmentation. In *2019 9th International Conference on Computer and Knowledge Engineering (ICCKE)* 2019; pp 269−275.

(50) Zhou, H.-Y.; Guo, J.; Zhang, Y.; Han, X.; Yu, L.; Wang, L.; Yu, Y. nnFormer: volumetric medical image segmentation via a 3D transformer. *IEEE Trans. Image Process.* **2023**, *32*, 4036−4045.